JOURNAL OF GEOPHYSICAL RESEARCH, VOL. 106, NO. A9, PAGES 18,895–18,905, SEPTEMBER 1, 2001

# Energetic ion dynamics in Jupiter's plasma sheet

R. S. Selesnick
The Aerospace Corporation, Los Angeles, California

C. M. S. Cohen
California Institute of Technology, Pasadena, California

K. K. Khurana
Institute of Geophysics and Planetary Physics, University of California, Los Angeles, California

**Abstract.** A systematic study of energetic ion trajectories in Jupiter's plasma sheet region predicts a significant role for both regular and stochastic types of motion and reveals several aspects of the ion dynamics that aid in the interpretation of Galileo observations. The motion is generally confined to the vicinity of the current sheet in a way that is proportional to the variable current sheet thickness as seen in the particle and field data. The radial extent of the trajectories increases with rigidity and initial radial distance from the planet, explaining the corresponding lack of high-rigidity ions and decreasing radial gradients at lower rigidity. Ion intensity increases associated with changes in current sheet thickness suggest an acceleration region at ~25 to 30 $R_J$. Energy dispersion in ion events at larger radial distances can be explained by such a source combined with elastic ion scattering.

## 1. Introduction

Models of Jupiter's magnetic field based on data from the Pioneer and Voyager spacecraft showed that the planetary dipole is distorted by current flowing in the extended plasma sheet that is the dominant feature of Jupiter's magnetosphere [*Goertz et al.*, 1976; *Connerney et al.*, 1981]. Observations of energetic particles showed that, beyond the inner radiation zone, they are also substantially confined to the vicinity of the plasma sheet [e.g., *Vogt et al.*, 1979]. More recent results from the Galileo orbiter have confirmed these essential properties and also shown that the magnetosphere is highly dynamic, with substantial variability in both fields and particles on timescales of hours and days [*Louarn et al.*, 1998; *Woch et al.*, 1998; *Russell et al.*, 1999; *Mauk et al.*, 1999].

The composition of energetic, several MeV/nucleon, ions in Jupiter's inner magnetosphere (largely oxygen and sulfur) and their low ionization states imply that their origin is the moon Io, while their composition in the plasma sheet region (largely oxygen and carbon) implies a solar origin [*Vogt et al.*, 1979; *Garrard et al.*, 1996; *Cohen et al.*, 2000]. Ionization of neutral gas from Io produces a plasma that is transported radially outward [*Belcher*, 1983], but radial gradients of the energetic ions show that they are transported inward toward Io [*Gehrels and Stone*, 1983]. Therefore ion acceleration must occur outside this region, possibly in the plasma sheet beyond radial distances of ~15 $R_J$ [*Barbosa et al.*, 1984]. Galileo has provided an opportunity to directly identify the acceleration site by making ion measurements on multiple passes through the plasma sheet region, but reliable interpretation of these data requires an understanding of the ion dynamics.

Jupiter's distended plasma sheet magnetic field configuration is similar to that of the Earth's magnetotail for which the ion dynamics have been studied in detail by numerical trajectory computations (see review by *Chen* [1992]). The trajectories at Jupiter can therefore be classified in a similar way [*Cheng and Decker*, 1992]. Previous studies of ion motion in Jupiter's plasma sheet have emphasized local aspects such as pitch angle diffusion [*Birmingham*, 1984] and the interpretation of measured ion anisotropies [*Cheng and Decker*, 1992; *Drolias et al.*, 1996]. However, interpretation of the dynamical nature of the Galileo ion observations requires a systematic study of ion trajectories emphasizing their large scale properties. In this work we begin such a study following a brief survey of some Galileo ion data.

## 2. Observations

Data from the Galileo heavy ion counter (HIC) [*Garrard et al.*, 1992] are shown in Figure 1. They were taken in 1997 during the ninth and tenth Galileo orbits (C9 and C10). The 12 days of data from each orbit are centered approximately on the closest approach to Jupiter and shown as a function of spacecraft event time (SCET), radial distance from Jupiter in planetary radii ($R_J$), and local time (LT). Two single-detector count rates, LB2 and LB3, respond to all species of energetic ions; and a multidetector detector count rate, LETB, responds only to heavy ions ($Z > 5$). The response characteristics to significant ion species are summarized in



Paper number 2000JA000242.
0148-0227/01/2000JA000242$09.00

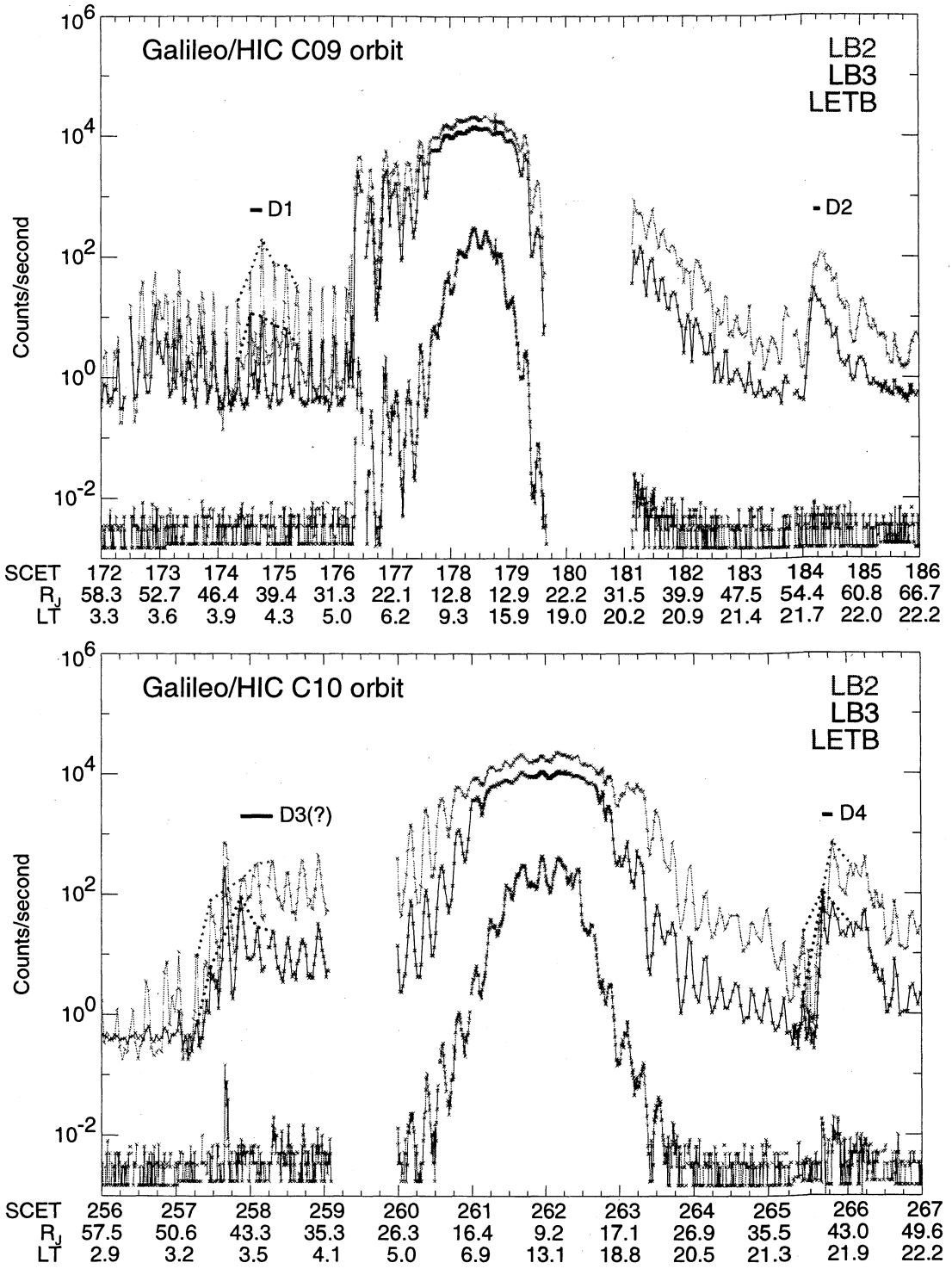


**Figure 1.** Energetic ion counting rates versus time measured by the heavy ion counter (HIC) on Galileo from consecutive orbits in 1997. The rates from top to bottom are LB2 (mostly 2 to 6 MeV protons), LB3 (mostly 5 to 11 MeV protons), and LETB (mostly 4 to 18 MeV/nucleon oxygen). The horizontal bars labeled D1 to D4 and the dotted lines highlight the dispersive events described in the text.

Table 1. The count rates shown in Figure 1 are generally proportional to ion intensity (except for rates $\gtrsim 10^4$ counts/s where some saturation occurs).

Several significant properties of the plasma sheet energetic ions are evident from the figure. First, it is clear that planetward of at least ~20 $R_J$ the ion intensities generally increase toward Jupiter. This is the typical radiation belt observation by a detector with a fixed energy threshold resulting from adiabatic heating as particles are transported planetward. We are primarily concerned with ions observed in the plasma sheet region beyond ~20 $R_J$. In this region the data are not clearly organized by radial distance. An

**Table 1.** Heavy Ion Counter Geometry Factors $G$ and Approximate Energy Ranges for Selected Elements

| | LB2 | LB3 | LETB[a] |
|---|---|---|---|
| $G$, cm$^2$ sr | 0.42 | 0.57 | 0.42 |
| H, MeV | 2–6 | 5–11 | – |
| C, MeV/nucleon | >3.5 | >4 | 3.5–15 |
| O, MeV/nucleon | >4 | >5 | 4–18 |
| S, MeV/nucleon | >5 | >6 | 5–25 |

[a] The LETB rate requires a two-detector coincidence and has a lower energy threshold than the nominal three-detector coincidence requirement [*Garrard et al.*, 1992].

obvious feature is the 5-hour periodicity in the ion intensities resulting from the Galileo orbit being crossed by the plasma sheet twice per 10-hour Jovian rotation period as a result of the 10° tilt of Jupiter's dipole axis. The periodicity shows that the ions are concentrated at the center of the plasma sheet, but the amplitude of the modulation, and therefore the characteristic thickness of the sheet in which the ions are concentrated, is variable. The sheet is thinner on both inbound orbits, which occur in the morning sector, than on the outbound orbits, which occur in the late evening sector. This trend is seen in most, but not all, of the other Galileo orbits, but the HIC data were most complete in the C9 and C10 orbits. Transitions in sheet thickness can be sudden, as on days 176 and 257 when the sheet thickness increased in association with increases in ion intensities. Close-ups of the data from these two periods, along with data from the Galileo magnetometer [*Kivelson et al.*, 1992], are shown in Figures 2 and 3. Changes in the current sheet thickness are seen in the magnetic field magnitude, as are nearby field fluctuations indicative of plasma turbulence. The magnetic

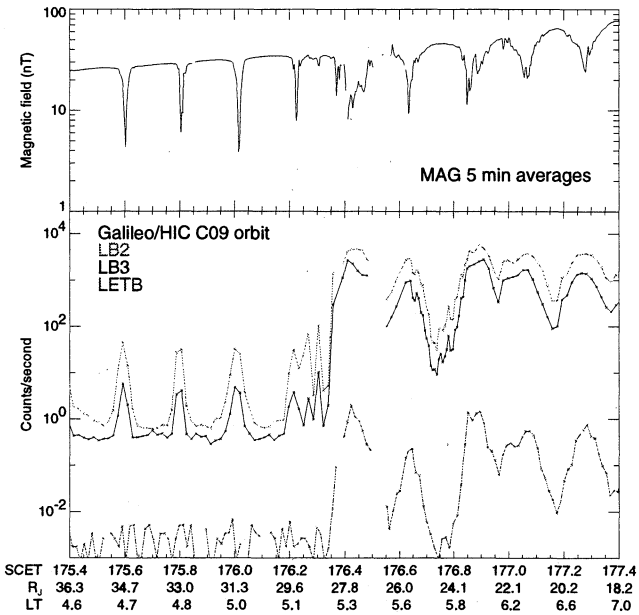


**Figure 2.** Energetic ion and magnetometer data from the C9 orbit.

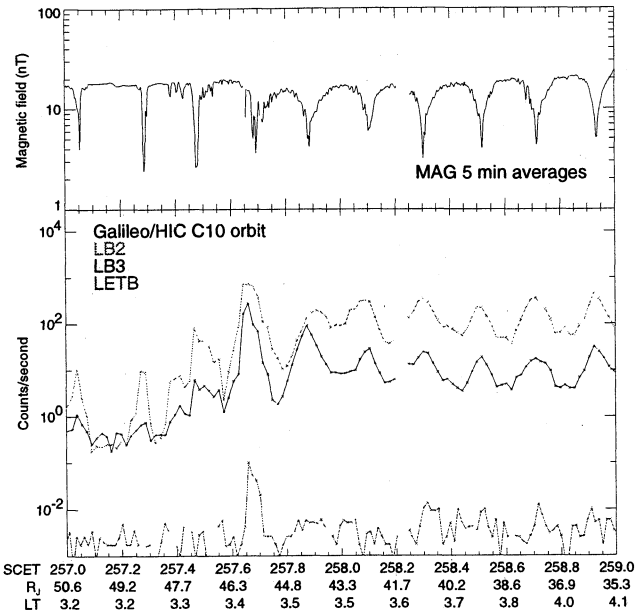


**Figure 3.** Energetic ion and magnetometer data from the C10 orbit.

field components (not shown) confirm that Galileo continued to cross the current sheet throughout the periods shown in Figure 1.

Ion intensity increases, such as those on days 184 and 265 (Figure 1), typically occur quickly (hours) and decay slowly (days). The decay of similar events on the inbound orbits, such as beginning on days 176 and 257, can be obscured by the generally increasing ion intensities with the approach to Jupiter, and their overall shape can be obscured by the modulation from the thinner inbound current sheet. Smaller such events can be seen in the thin current sheet on days 172 and 174, but the intensity increases appear less rapid.

The events on days 184 and 265 (Figure 1) show clear energy dispersion, in which high energies appear sooner, suggestive of particles arriving from a distant source. The day 174 event also shows some energy dispersion if only the envelopes of the modulated intensities are considered. The horizontal bars in Figure 1 labeled D1, D2, and D4 show the time periods between the arrival of the peak high-energy (LB3) and low-energy (LB2) rates for these dispersive events. The dotted lines show the envelopes of the modulated rates for the events where the dispersion is defined only by those envelopes. Such dispersive features at lower particle energies have been associated with quasi-periodic reconfigurations of the magnetosphere [*Woch et al.*, 1998]. Some intensity increases in the HIC data, such as the one on day 176 (Figure 2) that is closer to Jupiter, do not show energy dispersion. The increase on day 257, labelled D3 in Figure 1 and also shown in Figure 3, has a nondispersed peak intensity but, excluding that peak from the intensity envelopes as shown by the dotted lines, may be dispersive on a longer timescale. In general, the dispersive features can be observed only on timescales longer than 5 hours because of the modulation in the data due to the current sheet crossings.

The combination of magnetic field and energetic ion data (Figures 2 and 3) shows that a change in current sheet thickness causes a corresponding change in the ion confinement. Associated energy-dispersed changes in ion intensity suggest that the changes were initiated at a location remote from the observation site. Lack of dispersion in the ion features seen in the ~25 to 30 $R_J$ region (day 176 in Figures 1 and 2 and similar features in other orbits not shown) suggests that this region is the site of the changes in sheet thickness and the primary ion acceleration site.

Many features seen in the LB2 and LB3 rates are not apparent in the LETB rate (Figure 1), so those features must be formed primarily by protons, although they could be present in the heavy ions at energies below the LETB threshold. A subset of the counts that form the LETB rate can be analyzed for composition [*Cohen et al.*, 2000]. Plasma sheet features in these rates, such as the enhancements on days 176 and 257, have a solar composition, with comparable oxygen and carbon abundances, in agreement with previous composition measurements in this region [*Vogt et al.*, 1979]. The nearly constant background rate seen in the multidetector LETB rate is caused by cosmic rays that are not trapped in the magnetosphere.

While the composition of the accelerated heavy ions is solar as described above, plasma sheet ions observed by Voyager and Galileo at lower energy (~10 keV to 1 MeV total kinetic energy) [*Kane et al.*, 1999] have an Io-like composition (S and O). Their acceleration at the sites of plasma sheet thinning and subsequent inward radial diffusion may be the source of the energetic sulfur and oxygen ions observed in the inner magnetosphere. Ionization of fast neutral atoms produced by charge exchange in the Io torus can also provide a seed population for accelerated ions [*Barbosa et al.*, 1984]. Smaller-scale nondispersive ion features concurrent with plasma sheet thinning and magnetic field fluctuations are observed beyond 30 $R_J$ (e.g., day 257.6 in Figures 1 and 3), suggesting that acceleration sites may be transported by outward plasma flow from their more common location.

The plasma sheet thinning may be caused by an outward release of plasma [*Russell et al.*, 1999] in a similar way to the thinning of the terrestrial plasma sheet following plasmoid release during a magnetic substorm. Unlike terrestrial substorms the plasma sheet thinning events do not appear to be initiated by reconnection across the plasma sheet [*Russell et al.*, 1999], nor do they appear to be related to the small-scale flux tube interchange events [*Kivelson et al.*, 1997] that are thought to transport plasma outward from the Io plasma torus. They may represent a decoupling of the plasma from the magnetic field, caused by anomalous resistivity, that allows the plasma to move outward across the field and returns the field to a less distorted and more dipolar state [*McNutt et al.*, 1987]. These events may be quasi-periodic with an intrinsic timescale of ~3 days, as suggested by *Woch et al.* [1998]. Jovian energetic events seen in plasma waves with a similar period [*Louarn et al.*, 1998] may be related to the same phenomenon. Particle injections, associated with such field dipolarizations in the terrestrial case, have been observed at Jupiter throughout the radial distance range of ~10 to 25 $R_J$ [*Mauk et al.*, 1999], although no association has been made with the plasma sheet thinning events.

Much of the above discussion is based on the particle and field data in only a qualitative way. The primary goal in this work is to characterize the energetic ion trajectories in the plasma sheet region by numerical calculation. A secondary goal is to determine whether they support or refute our interpretations of the ion data.

## 3. Magnetic Field Models

An accurate magnetic field model is critical to obtaining realistic ion trajectories. The results of the last section showed that the model should include a variable current sheet thickness. We have adopted the Euler potential model of *Khurana* [1997] using the parameters derived from both Voyager and Pioneer data, but with some modifications. The model includes a parameter $d_1 = 2\ R_J$ that represents the characteristic thickness of the current sheet. We have changed this to values of 1 and 3 $R_J$ to represent the thin and thick current sheets, respectively. Most of our calculations are done with the 1 $R_J$ value. The magnetic field data show that when the sheet thickness changes, the total current flowing in the sheet remains approximately constant. The total sheet current is maintained at the original model value by changing the model parameter $B_1$ by the same factor as the change in the sheet thickness parameter $d_1$. Some representative field lines with the thin sheet model are shown in Figure 4. The sweepback of the field lines due to Jupiter's rotation, the dipole tilt relative to the rotation axis, and the hinging of the current sheet due to the solar wind flow are evident.

An additional modification of the magnetic field model that simplifies the interpretation of ion trajectories is to as-

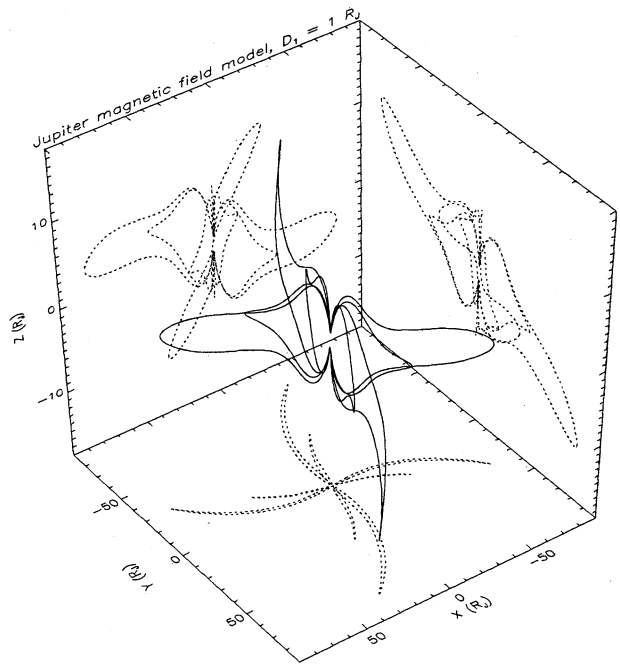


**Figure 4.** Perspective view of selected magnetic field lines with the full magnetic field model and thin current sheet in system III coordinates. The field lines are also projected on the $X$-$Y$, $X$-$Z$, and $Y$-$Z$ planes (dotted lines). Jupiter's spin phase is such that the magnetic dipole is tilted toward the direction of the solar wind flow. Note the expanded scale in the $Z$ coordinate.

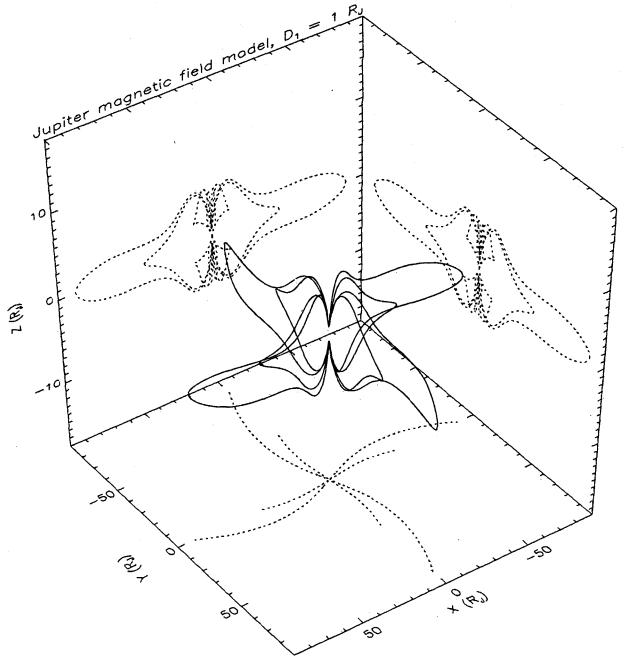


**Figure 5.** Similar to Figure 4, but with the simplified field model.

sume that Jupiter's internal magnetic field is a simple dipole whose moment is aligned with Jupiter's rotation axis and perpendicular to the solar wind flow. Representative field lines in this case, again with the thin sheet model, are shown in Figure 5. Now the magnetic field is azimuthally symmetric with respect to the rotation axis and there is no hinging of the current sheet. We call this the simplified field model and use it for most of the ion trajectory calculations. Although the magnetic field configurations represented in Figures 4 and 5 are quite different, the local magnetic field properties at similar locations relative to the current sheet are not. This justifies the use of the simplified model for calculating ion trajectories, as we demonstrate later.

## 4. Trajectory Simulations

We solve the equation of motion for a charged particle in Jupiter's magnetic field **B** in the form

$$\mathcal{R}\frac{d\mathbf{t}}{ds} = \mathbf{t} \times \mathbf{B}, \tag{1}$$

where $\mathbf{t} = d\mathbf{r}/ds$ is the tangent to the trajectory at position **r**, $s$ is the path length along the trajectory, and $\mathcal{R} = p/q$ is the particle's rigidity or momentum $p$ per charge $q$. Electric field and other forces are not included, as is valid for sufficiently high particle speeds, so the shape of the trajectory depends only on $\mathcal{R}$. The equation of motion (1) is solved numerically by a fourth-order Runge-Kutta method with adaptive step sizes. The conservation of energy in (1) is monitored by verifying $|\mathbf{t}| = 1$ to ensure the accuracy of the integration. In the case of the simplified magnetic field model, which is independent of azimuth, the component along the symmetry axis of the generalized angular momentum is also conserved by (1) and its conservation in the numerical integration is also verified.

A sample ion trajectory in the simplified magnetic field model with thin current sheet is shown in Figure 6. This is a regular, or integrable, trajectory that executes a relatively simple oscillatory motion across the current sheet of the type first described by *Speiser* [1965]. It orbits the planet three times in the 1.23-hour simulation time shown and never exits the current sheet region. The oscillatory motion can be understood as gyration about the radial component of the magnetic field, but before a gyro-orbit can be completed, the trajectory crosses the neutral sheet into the opposed radial field where it begins to gyrate in the opposite sense. This is combined with azimuthal drift around Jupiter caused by gyration about the weak magnetic field component perpendicular to the neutral sheet.

Another ion trajectory is shown in Figure 7. This had the same initial conditions, at the equatorial plane, as the trajectory in Figure 6, but the thick current sheet field model was used. The general characteristics of the two trajectories are the same, with the second one having a larger radius of curvature owing to the weaker field of the thick current sheet. This similarity between trajectories in the simplified field model with different sheet thicknesses is generally valid because the normal component of the magnetic field at the neutral sheet does not vary with the sheet thickness. In fact, it also does not vary with changes in the total sheet current, so that increasing or decreasing that current has a similar effect on the ion motion to increasing or decreasing the sheet thickness. In reality, however, the normal component of the magnetic field, which depends largely on the radial gradient of the sheet current, clearly can vary, so that the calculated ion trajectories should be considered as only representative.

We now compare the trajectory of Figure 6 with a similar one in the full magnetic field model. Here it is difficult to

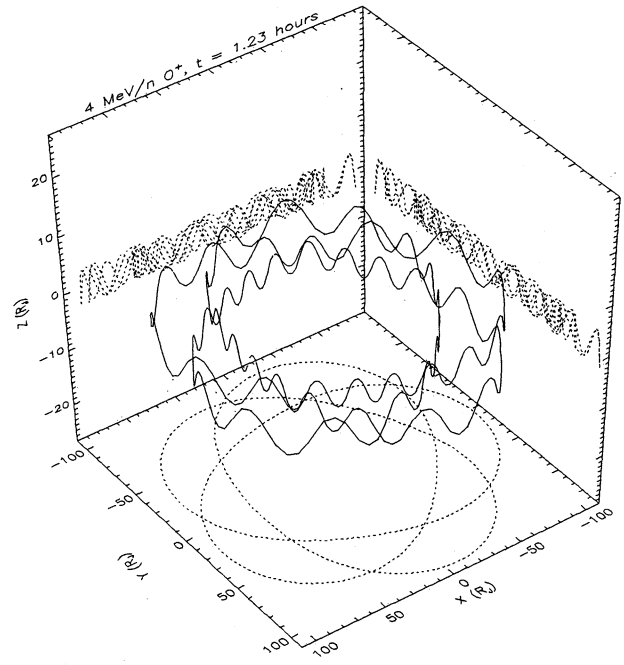


**Figure 6.** Perspective view of a regular ion trajectory in the simplified magnetic field model with thin current sheet. The trajectory is also projected on the $X$-$Y$, $X$-$Z$, and $Y$-$Z$ planes (dotted lines). The rigidity $\mathcal{R}$ and simulation time $t$ correspond to a 4 MeV/nucleon $O^+$ ion. The angular momentum $Z$-component per charge is $\mathcal{L} = 864$ GV $R_J$.

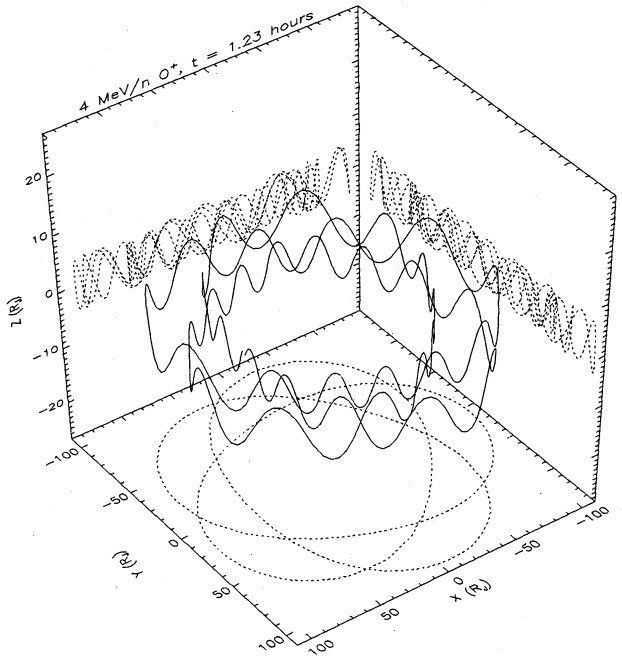


**Figure 7.** Similar to Figure 6, but with the thick current sheet.

determine an equivalent set of initial conditions because of the warped current sheet. We chose to start the trajectory at the minimum magnetic field location on a field line with the same cylindrical distance from the rotation axis and with the same pitch and gyrophase angles relative to the field direction as were used in the simplified field at the neutral sheet. The resulting trajectory is shown in Figure 8.

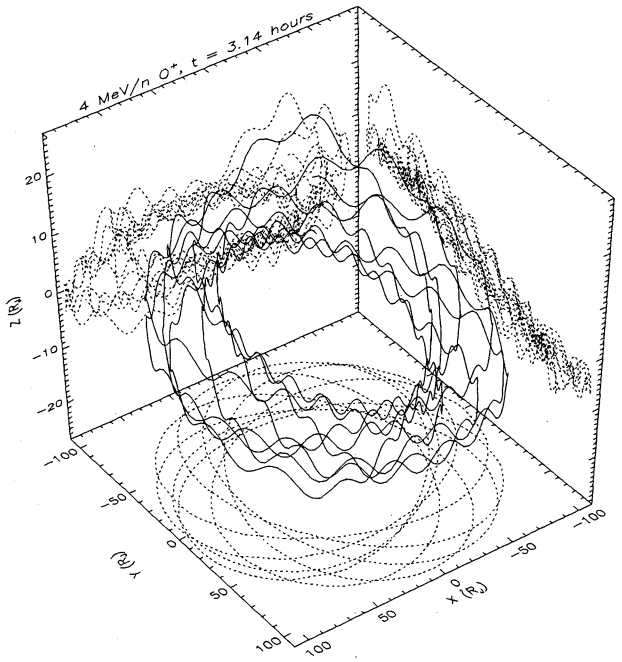


**Figure 8.** Similar to Figure 6, but in the full magnetic field model with thin current sheet, a longer simulation time, and shown in system III coordinates. At the beginning of the simulation the magnetic field was in the same orientation as shown in Figure 4.

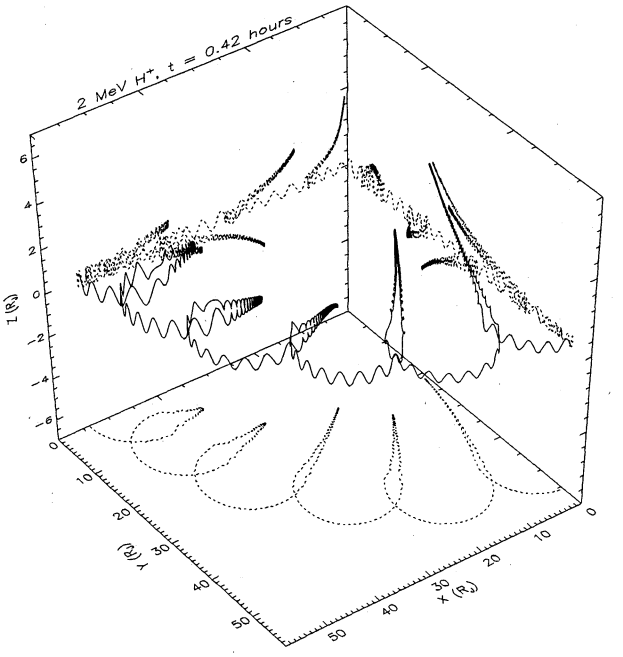


**Figure 9.** Perspective view of a stochastic ion trajectory in the simplified magnetic field model with thick current sheet. The rigidity $\mathcal{R}$ and simulation time $t$ correspond to a 2 MeV proton. The angular momentum $Z$ component per charge is $\mathcal{L} = 806$ GV $R_J$.

The trajectory is again confined to the vicinity of the current sheet, which is now warped as shown in Figure 4. The important points are that the trajectories again have the same basic characteristic, oscillation across the current sheet, and are confined to the same radial range. The full magnetic field model is not azimuthally symmetric, so that there is no second integral of the motion equivalent to the generalized angular momentum component that is conserved in the simplified case. However, the trajectory in Figure 8, which was followed for eight full orbits, shows that there is no essential difference from the simplified field model case. The same result is obtained from trajectories with different initial conditions. Therefore we can take advantage of the extra integral of the motion in the simplified case to describe the ion trajectories. This conclusion is a result of the similar local properties of the two field models on scale size of the trajectory, which is determined by the ion rigidity. The value of the rigidity is the largest one we will consider, so the same conclusion applies to all of the cases discussed below.

A final example of a single ion trajectory is shown in Figure 9. In this and all subsequent calculations the simplified field model is used. The initial conditions correspond to a lower rigidity than in the previous cases, resulting in a smaller scale size. The trajectory, which was followed for a quarter of an orbit, includes segments where it oscillates across the current sheet as in the previous cases and other segments where it moves out of the current sheet into the stronger field region above or below until it is eventually reflected back by the increasing field strength. Because the direction of motion is randomized each time the ion enters the current sheet, the segment lengths are variable, and this is an example of a stochastic trajectory.

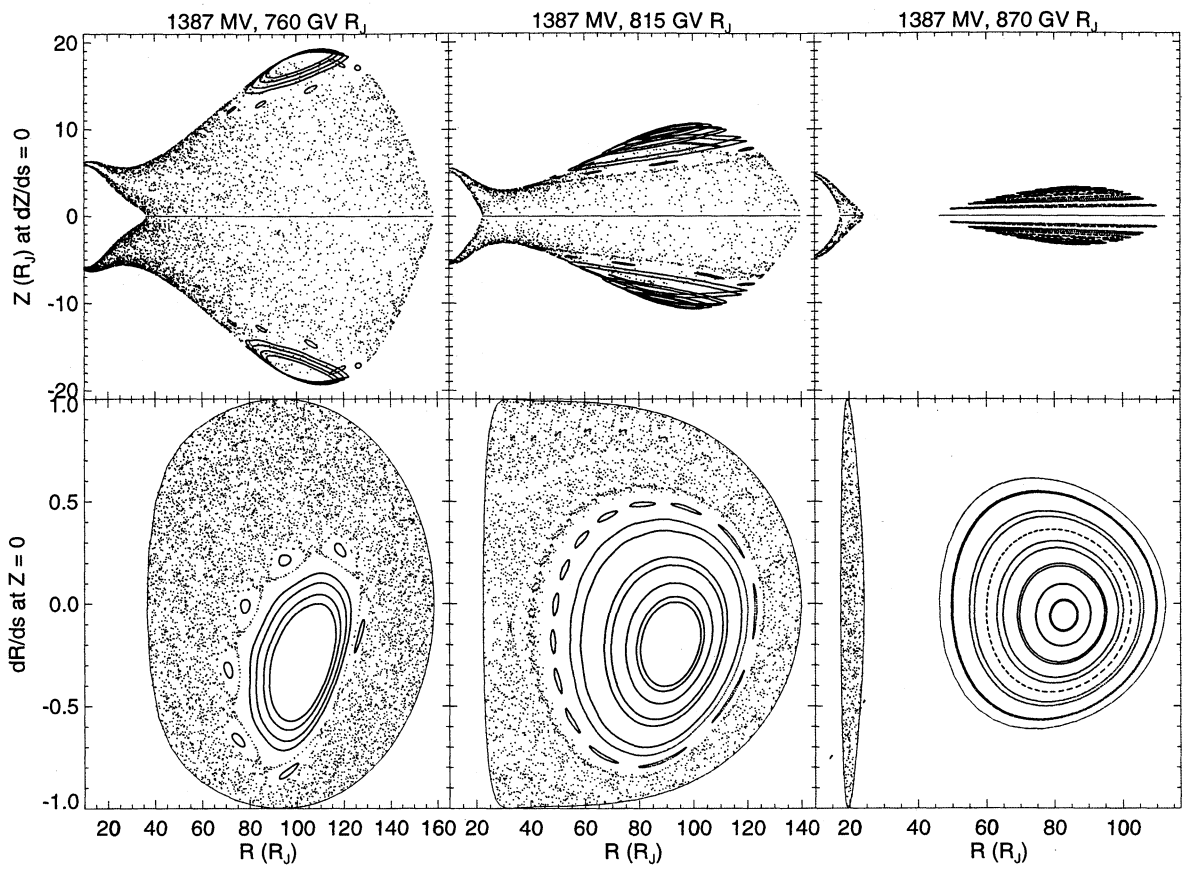


**Figure 10.** Poincaré surface-of-section maps for energetic ions of high rigidity $\mathcal{R}$ and three different $Z$ components of angular momentum per charge $\mathcal{L}$.

We are now in a position to provide a more systematic description of the ion trajectories. We make use of the property that the significant trajectory characteristics can be inferred from numerical integration in the simplified field model. Then the trajectories are organized by two integrals of the motion for which we choose the rigidity $\mathcal{R}$ and the component of the generalized angular momentum per charge along the $Z$ axis $\mathcal{L} = R(A_\phi + \mathcal{R}\sin\alpha\sin\beta)$, where $R$ is cylindrical radius, $A_\phi$ is the azimuthal component of the magnetic vector potential, $\alpha$ is the pitch angle, and $\beta$ is the gyrophase angle. The extent and general properties of the trajectories can be most easily inferred from Poincaré surface-of-section maps [*Lichtenberg and Lieberman*, 1983; *Chen*, 1992], which show the intersections of the trajectory with a given plane in phase space. Poincaré maps in the $R$, $dR/ds$ plane at $Z = 0$ and the $R$, $Z$ plane at $dZ/ds = 0$ for selected $\mathcal{R}$ and $\mathcal{L}$ values are shown in Figures 10, 11, and 12.

Each map contains several trajectories, each followed for many orbits around the planet, with equal $\mathcal{R}$ and $\mathcal{L}$ values but different initial conditions. The initial conditions were selected at $Z = 0$, at equally spaced radii $R$, and at gyrophase angles $\beta$ of 90° and 270° relative to the radial direction. The required initial pitch angle $\alpha$ for each trajectory was then calculated from the $\mathcal{R}$ and $\mathcal{L}$ values. For each $\mathcal{R}$ and $\mathcal{L}$ value there is a range of allowed radial locations that can be calculated directly from the definition of $\mathcal{L}$. To facilitate a comparison of the ion trajectory results with the data shown in the last section, we show in Table 2 some examples of the relationship between rigidity and energy per nucleon for ions of different charge states.

Several properties of the ion trajectories can be inferred directly from the Poincaré maps. Both regular and stochastic trajectories are evident at each rigidity. The regular trajectories, confined to surfaces in phase space that appear as closed curves on the Poincaré maps, are more prevalent at higher rigidities $\mathcal{R}$ and lower angular momentum $Z$ components $\mathcal{L}$. Each of the concentric closed curves represents a single regular trajectory, while each sequence of closed curves around the outer edge of the concentric ones in Figure 10 (lower $\mathcal{L}$ values) also represent a single trajectory. They remain in or near the current sheet because they consist only of the oscillatory motion, an example of which is shown in Figure 6. The bounding curve around each map in the $R$, $dR/ds$ plane is a special regular trajectory that is confined to the equatorial ($Z = 0$) plane. The stochastic trajecto-

**Table 2.** Energy per Nucleon $E$ for Selected Ions of Given Rigidity

| Rigidity, MV | $H^+$ $E$, MeV | $O^{8+}$ $E$, MeV/nucleon | $O^+$ $E$, MeV/nucleon |
|---|---|---|---|
| 61.3 | 2. | 0.5 | 0.0078 |
| 173.5 | 16. | 4. | 0.063 |
| 1387.0 | 725. | 229. | 4. |

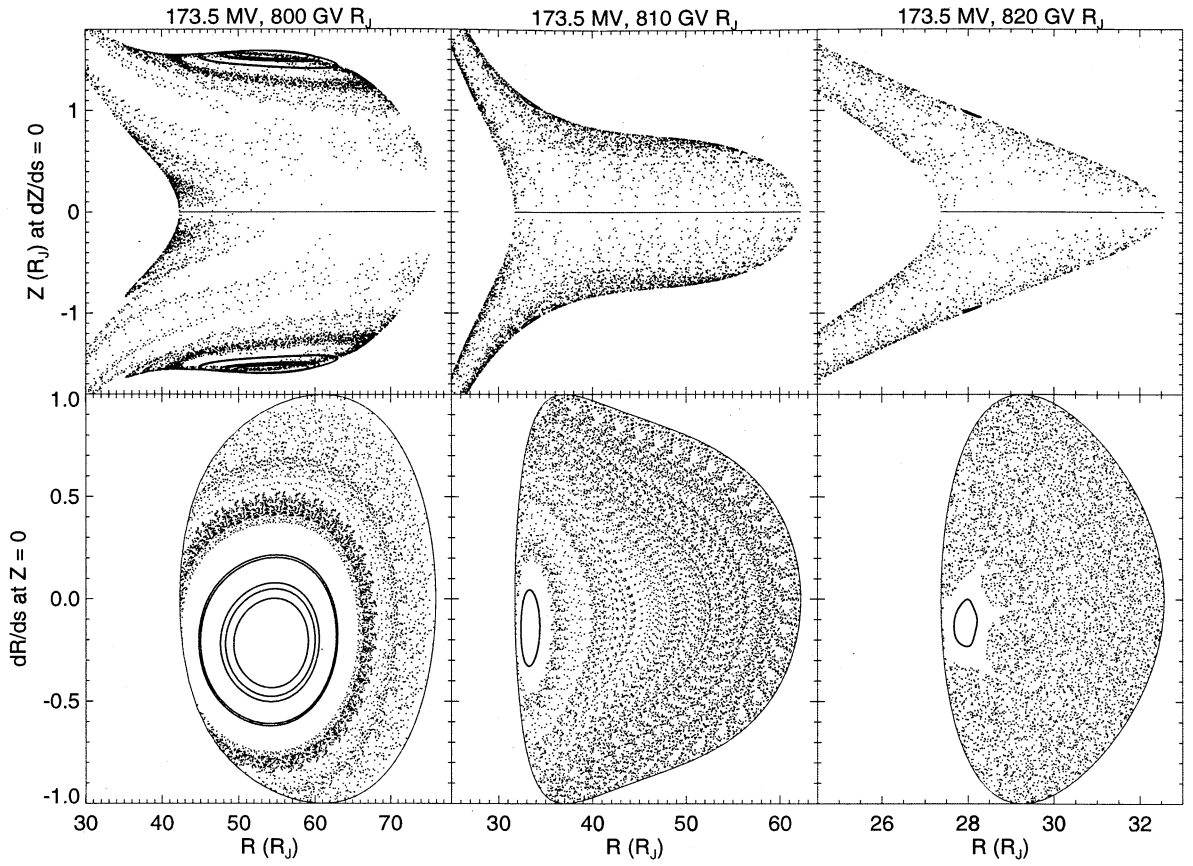


**Figure 11.** Poincaré surface-of-section maps for energetic ions of medium rigidity $\mathcal{R}$ and three different $Z$ components of angular momentum per charge $\mathcal{L}$.

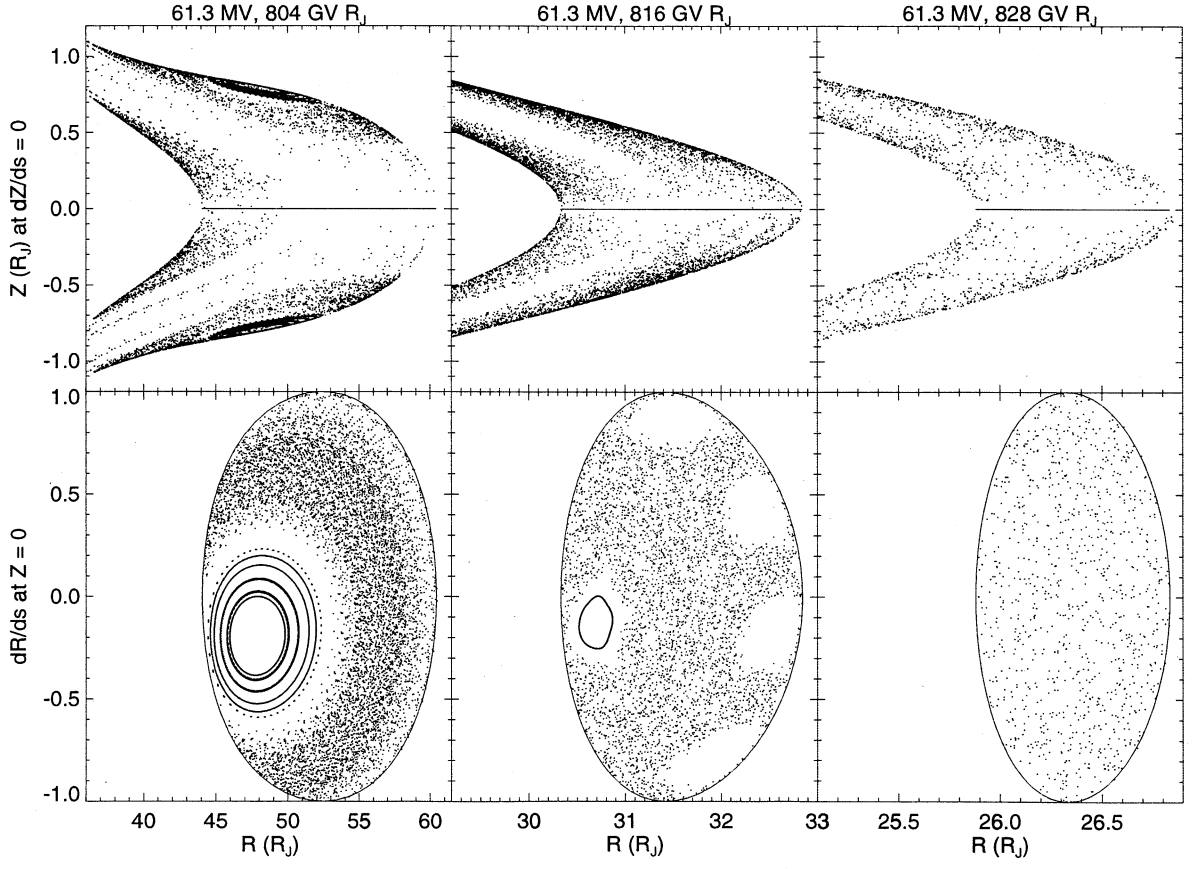


**Figure 12.** Poincaré surface-of-section maps for energetic ions of low rigidity $\mathcal{R}$ and three different $Z$ components of angular momentum per charge $\mathcal{L}$.

ries, that densely fill volumes of phase space appearing as bounded areas on the Poincaré maps, are more prevalent at lower $\mathcal{R}$ or higher $\mathcal{L}$. They generally include both outer current sheet segments and inner field-aligned segments, as shown by the example in Figure 9. The stochastic regions usually surround the regular trajectory regions, although in the high $\mathcal{R}$ (Figure 10) and high $\mathcal{L}$ example they are separated. The stochastic regions can be filled by a single trajectory, although several are included because in some cases it may take a long time for a single trajectory to reach less densely filled areas (as seen by variations in density at lower $\mathcal{R}$ values). Only one stochastic trajectory was included at $\mathcal{L} = 816$ GV $R_J$ in Figure 12 to clearly show the transient regions [*Chen*, 1992] near the outer edge, but these are not a significant feature in most of the trajectories. The regular trajectories are less clearly apparent in the $R$, $Z$ plane where they overlap with the stochastic trajectories. The regular and stochastic regions are always separated in the $R$, $dR/ds$ plane. The radial extent of each Poincaré map, which was determined prior to the trajectory calculations as described above, increases with $\mathcal{R}$ and decreases with $\mathcal{L}$, as does the thickness of the sheet to which the trajectories are confined. The field-aligned trajectory segments, where the stochastic regions separate above and below $Z = 0$ in the $R$, $Z$ maps, are generally confined within $\sim$40 $R_J$. The radial excursions of the stochastic trajectory current sheet segments decrease with $\mathcal{L}$, so that at the highest $\mathcal{L}$ values the motion consists only of field-aligned segments and pitch angle randomization in the current sheet. Pitch angle diffusion coefficients for these type of trajectories were calculated analytically by *Birmingham* [1984].

Many of the results from the trajectory simulations can be related directly to features in the ion data. However, before discussing such comparisons, we consider the dispersive ion events with another type of simulation.

## 5. Dispersive Event Simulation

The dispersive events seen in the HIC data are most simply interpreted as due to time-of-flight differences from a remote ion source. The events are seen in the single-detector rates that respond primarily to 2 and 6 MeV protons. Accurate values for the flight time differences are obscured somewhat by the 5-hour modulation, but they are generally a few hours. The event that begins on day 184 is perhaps the clearest because the 5-hour modulation is minimal owing to a thick current sheet (the sheet thickened at the start of the event). In this case the maximum 6 MeV proton rate arrived at Galileo $\sim$2.5 hours before the maximum 2 MeV proton rate. This time difference corresponds to a total path length from a common source of 6000 $R_J$ and total flight times of 3.5 hours for the 6 MeV protons and 6 hours for the 2 MeV protons. Comparing with Figure 9, we see that these times generally are sufficient for a few complete orbits of Jupiter and many traversals between the inner and outer radial extent of each trajectory. Therefore the timescale of dispersive events is too long for them to have been formed by direct access to an ion source with the type of trajectories we have considered so far. That is, the different speeds of ions moving along their trajectories from a remote source could not create the amount of dispersion seen in the data. If the number of degrees of freedom in the integration were increased from 2, as in the simplified magnetic field model, to 3, as in the full field model, then the surfaces over which the particles move in phase space are no longer separated and trajectories can move between them in a process known as Arnold diffusion [e.g., *Lichtenberg and Lieberman*, 1983]. However, calculations of the type represented in Figure 8 show that this process is too slow to account for the dispersive features and something else is required.

Scattering from magnetic field fluctuations is one process that can change the angular momentum component value $\mathcal{L}$ and cause enhanced radial transport. It can be effective at changing the radial access of the ion trajectories because of the significant overlap in the radial extents of the trajectories with different $\mathcal{L}$ values, as shown in the last section. We can illustrate this by a Monte Carlo simulation. The events are typically observed near 50 $R_J$ from Jupiter (Figure 1). By determining the radial range where a given $\mathcal{L}$ value is allowed, it is easy to show that the minimum radial distances at which 2 and 6 MeV protons have direct access to 50 $R_J$ are 38 and 34 $R_J$, respectively. Therefore the source region must be planetward of 34 $R_J$. For the Monte Carlo simulation we assume a source location of 30 $R_J$ in the equatorial plane, start ion trajectories from that location by sampling from an isotropic distribution, and count the number of trajectories crossing 50 $R_J$ as a function of time. Elastic scattering is included by modifying both the polar and azimuthal angles of the ion direction with angular changes sampled from a Gaussian distribution of mean $\sigma$. Trajectories can cross 50 $R_J$ multiple times but are removed from the simulation if they go beyond 80 $R_J$. Results from a 24-hour simulation with 300 trajectories each of 2 and 6 MeV protons with a mean square angular scattering rate of $\sigma^2/\delta t = 10^{-3}$ s$^{-1}$, where $\delta t = 10$ s is the simulation time between scattering events, are shown in Figure 13. They show that the 2 MeV proton intensity at 50 $R_J$ rises a few hours later than the 6 MeV proton intensity, as seen in the dispersive events. This is a result of the greater radial excursions of the 6 MeV

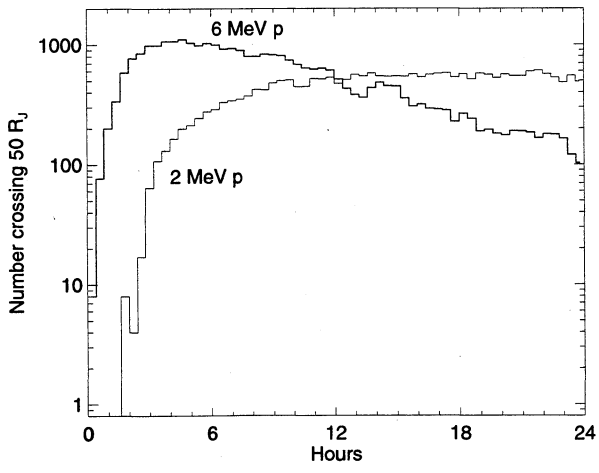


**Figure 13.** Simulated number of 2 and 6 MeV protons crossing 50 $R_J$ in each 0.4-hour period after 300 of each were started at 30 $R_J$ with isotropic distributions. Elastic scattering and losses at 80 $R_J$ are included as described in the text.

proton trajectories between scattering events. During the 24-hour simulation, 67 of the 300 2 MeV protons and 253 of the 300 6 MeV protons reached 80 $R_J$ and were lost. Clearly, these loss rates are not realistic and comparison with the data shows that a more equal loss rate between the two proton energies is perhaps required. Other details, such as the 5-hour modulation and changes in current sheet thickness, can also change the real shape of these events. However, the type of energy dispersion seen in the data can be reproduced by the simulation.

## 6. Conclusions

To aid in the interpretation of energetic ion data from Jupiter, we have made some numerical calculations of energetic ion trajectories in the plasma sheet region. We showed that a simplified magnetic field model is sufficient for describing the general trajectory characteristics and supports the use of Poincaré maps to aid in their classification. The trajectory simulations lend support to several aspects of our interpretation of the Galileo energetic ion observations:

1. The simulations show that the ions should be substantially confined to the vicinity of the current sheet for all initial conditions in agreement with the observations from Galileo and other spacecraft. The confinement scale height increases in proportion to the current sheet thickness.

2. The ion trajectories beyond ~30 $R_J$ from Jupiter cover a large radial extent, particularly at the higher rigidities. Therefore radial transport in this region is rapid and approximately conserves energy, in contrast to the adiabatic heating that accompanies radial transport planetward of at least ~20 $R_J$. This can account for generally decreased radial gradients observed in the energetic ion intensities beyond ~20 to 30 $R_J$.

3. High rigidity ions, such as 4 MeV/nucleon $O^+$, can be trapped on either stochastic or regular trajectories inside ~30 $R_J$, but beyond this radial distance the trajectories cover a large radial extent and ions on such trajectories are likely to be rapidly lost in the distant magnetosphere. This can explain why stably trapped high rigidity ions are observed only within ~30 $R_J$ and why the plasma sheet ion composition is different at high and low energies. It appears likely that the singly ionized energetic ions observed in Jupiter's inner magnetosphere with an Io-like composition were accelerated from a lower energy plasma sheet component in the ~25 to 30 $R_J$ region and then diffused inward.

4. At lower rigidities, such as 4 MeV/nucleon $O^{8+}$ and 2 MeV protons, the radial extent of the trajectories decreases, so that loss rates should be lower and stable trapping may extend farther from Jupiter. This can contribute to the predominance of solar energetic ions, which have higher ionization states than those from Io, in Jupiter's middle and outer magnetosphere.

5. The data beyond ~30 $R_J$ include many transient events, and energy dispersion in the more distant ones suggests that the source of these events was also in the ~25 to 30 $R_J$ region. The dispersion timescales are too long to be formed by direct access from a remote source. Monte Carlo simulations of ion count rates at 50 $R_J$, with a source of ions at 30 $R_J$, show that such dispersion can be produced if a specific rate of elastic scattering is included.

**Acknowledgments.** This work was supported by NASA grant NAG5-8634 under the Jovian System Data Analysis Program.

Janet G. Luhmann thanks the referees for their assistance in evaluating this paper.

## References

Barbosa, D. D., A. Eviatar, and G. L. Siscoe, On the acceleration of energetic ions in Jupiter's magnetosphere, *J. Geophys. Res., 89*, 3789–3800, 1984.

Belcher, J. W., The low energy plasma in the Jovian Magnetosphere, in *Physics of the Jovian Magnetosphere*, edited by A. J. Dessler, p. 68, Cambridge Univ. Press, New York, 1983.

Birmingham, T. J., Pitch angle diffusion in the Jovian magnetodisc, *J. Geophys. Res., 89*, 2699–2707, 1984.

Chen, J., Nonlinear dynamics of charged particles in the magnetotail, *J. Geophys. Res., 97*, 15,011–15,050, 1992.

Cheng, A. F. and R. B. Decker, Nonadiabatic particle motion and corotation lag in the Jovian magnetodisk, *J. Geophys. Res., 97*, 1397–1402, 1992.

Cohen, C. M. S., T. L. Garrard, and E. C. Stone, Io encounters past and present: A heavy ion comparison, *J. Geophys. Res., 105*, 7775–7782, 2000.

Connerney, J. E. P., M. H. Acuna, and N. F. Ness, Modeling the Jovian current sheet and inner magnetosphere, *J. Geophys. Res., 86*, 8370–8384, 1981.

Drolias, B., J. J. Quenby, A. Witcombe, A. Korth, E. Keppler, and J. B. Blake, Numerical simulations of non-adiabatic particle motions in the Jovian magnetosphere: Comparisons with Ulysses observations, *Planet. Space Sci., 44*(2), 153–161, 1996.

Garrard, T. L., N. Gehrels, and E. C. Stone, The Galileo heavy element monitor, *Space Sci. Rev., 60*, 305–315, 1992.

Garrard, T. L., E. C. Stone, and N. Murphy, Effects of absorption by Io on composition of energetic heavy ions, *Science, 60*, 393–394, 1996.

Gehrels, N., and E. C. Stone, Energetic oxygen and sulfur ions in the Jovian magnetosphere and their contribution to the auroral excitation, *J. Geophys. Res., 88*, 5537–5550, 1983.

Goertz, C. K., D. E. Jones, B. A. Randall, E. J. Smith, and M. F. Thomsen, Evidence for open field lines in Jupiter's magnetosphere, *J. Geophys. Res., 81*, 3393–3398, 1976.

Kane, M., D. J. Williams, B. H. Mauk, R. W. McEntire, and E. C. Roelof, Galileo energetic particles detector measurements of hot ions in the neutral sheet region of Jupiter's magnetodisk, *Geophys. Res. Lett., 26*, 5–8, 1999.

Khurana, K. K., Euler potential models of Jupiter's magnetic field, *J. Geophys. Res., 102*, 973–989, 1997.

Kivelson, M. G., K. K. Khurana, J. D. Means, C. T. Russell, and R. C. Snare, The Galileo magnetic field investigation, *Space Sci. Rev., 60*, 357–383, 1992.

Kivelson, M. G., K. K. Khurana, C. T. Russell, and R. J. Walker, Intermittent short-duration magnetic field anomalies in the Io torus: Evidence for plasma interchange?, *Geophys. Res. Lett., 24*, 2127–2130, 1997.

Lichtenberg, A. J., and M. A. Lieberman, *Regular and Stochastic Motion*, Springer-Verlag, New York, 1983.

Louarn, P., A. Roux, S. Perrout, W. Kurth, and D. Gurnett, A study of the large-scale dynamics of the Jovian magnetosphere using the Galileo plasma wave experiment, *Geophys. Res. Lett., 25*, 2905–2908, 1998.

Mauk, B. H., D. J. Williams, R. W. McEntire, K. K. Khurana, and J. G. Roederer, Storm-like dynamics of Jupiter's inner and middle magnetosphere, *J. Geophys. Res., 104*, 22,759–22,778, 1999.

McNutt, R. L, Jr., P. S. Coppi, R. S. Selesnick, and B. Coppi, Plasma depletions in the Jovian magnetosphere: Evidence of

transport and solar wind interaction, *J. Geophys. Res., 92*, 4377–4398, 1987.

Russell, C. T., D. E. Huddleston, K. K. Khurana, and M. G. Kivelson, Observations at the inner edge of the Jovian current sheet: Evidence for a dynamic magnetosphere, *Planet. Space Sci., 47*, 521–527, 1999.

Speiser, T. W., Particle trajectories in model current sheets, 1, Analytical solutions, *J. Geophys. Res., 70*, 4219–4226, 1965.

Vogt, R. E., et al., Voyager 1: Energetic ions and electrons in the Jovian magnetosphere, *Science, 204*, 1003–1007, 1979.

Woch, J., N. Krupp, A. Lagg, B. Wilken, S. Livi, and D. J. Williams, Quasi-periodic modulations of the Jovian magnetotail, *Geophys. Res. Lett., 25*, 1253–1256, 1998.

C. M. S. Cohen, California Institute of Technology, Pasadena, CA 91125.

K. K. Khurana, Institute of Geophysics and Planetary Physics, University of California, Los Angeles, CA 90095.

R. S. Selesnick, The Aerospace Corporation, P. O. Box 92957-M2/259, Los Angeles, CA 90009. (richard.s.selesnick@aero.org)

(Received June 21, 2000; revised October 25, 2000; accepted November 16, 2000.)